

# Observational signatures of rotating black holes in the semiclassical gravity with trace anomaly

Zhenyu Zhang<sup>1</sup>, Yehui Hou<sup>1\*</sup>, Minyong Guo<sup>2</sup>

<sup>1</sup>*Department of Physics, Peking University, No.5 Yiheyuan Rd, Beijing 100871, P.R. China*

<sup>2</sup>*Department of Physics, Beijing Normal University, No.19, Xijiekouwai St, Beijing 100875, P. R. China*

## Abstract

In a recent work by Fernandes [1], an exact stationary and axisymmetric solution was discovered in semiclassical gravity with type-A trace anomaly, identified as a quantum-corrected version of the Kerr black hole. In this study, we explore the observational signatures of this black hole solution. Our investigation reveals that there exist prograde and retrograde light rings, whose radii increase monotonically with the coupling parameter  $\alpha$ . We also observe that when  $\alpha$  is negative, the shadow area for the quantum-corrected black hole is smaller than that of the Kerr black hole, whereas when  $\alpha$  is positive, the area is larger. Furthermore, for a near-extremal black hole, its high-spin feature (the NHEKline) is found to be highly susceptible to disruption by  $\alpha$ . Moreover, we discuss the images of the quantum-corrected black hole in the presence of a thin accretion disk and compare them to those of the Kerr black hole. Our study highlights the importance of near-horizon emission sources in detecting the effects of quantum corrections by black hole images.

\* Corresponding author: yehuihou@pku.edu.cn

# 1 Introduction

Semiclassical gravity is an approach that considers the backreaction of quantum fields while treating spacetime classically. One of the quantum effects in this scheme is the trace anomaly, which refers to the breaking of symmetry in a conformally invariant classical theory due to one-loop quantum corrections [2]. As a result of the trace anomaly, the renormalized stress tensor of quantum fields has a non-zero trace, serving as a source term in the semiclassical Einstein equations. The trace anomaly may also induce higher-order curvature terms such as the Gauss-Bonnet term, which arises from the type-A anomaly [3].

One of the topics of solutions in semiclassical gravity is the corrected versions of classical black holes that account for quantum effects. However, the derivations are challenging because the renormalized stress tensor is often unknown, requiring additional assumptions to solve the problem. More than a decade ago, considering only the type-A anomaly, [4] was the first to find the static and spherically symmetric black hole solution in a four-dimensional spacetime within the framework of such semiclassical gravity. This spherically symmetric black hole has been widely studied in subsequent works [5–9] because of its intriguing features resulting from quantum effects. Furthermore, having an exact stationary and axisymmetric solution to the semiclassical Einstein equations that is sourced by the type-A trace anomaly is crucial for modeling the actual black hole in space.

Very recently, by adopting a Kerr-Schild ansatz with stationary and axisymmetric configuration, the author in [1] analytically solved the semiclassical Einstein equation and obtained a Kerr black hole solution with the type-A trace anomaly. Compared to the classical Kerr black hole, this new solution replaces the ADM mass with a mass function given by

$$\mathcal{M} = \mathcal{M}(r, \theta) = \frac{2M}{1 + \sqrt{1 - \frac{8\alpha r \xi M}{\Sigma^3}}}, \quad (1.1)$$

where  $M$  represents the ADM mass,  $\Sigma = r^2 + a^2 \cos^2 \theta$  with  $a$  denoting the spin parameter,  $\xi = r^2 - 3a^2 \cos^2 \theta$ , and  $\alpha$  representing the coupling constant of the type-A anomaly. This rotating black hole solution includes quantum corrections and reduces to the classical Kerr spacetime when  $\alpha = 0$ . Furthermore, when  $a = 0$ , the solution reduces to the static and spherically symmetric solution in semiclassical gravity. This new solution presents several unique characteristics. For instance, the event horizon geometry is non-spherically symmetric, and there exists another Killing horizon outside of it. Additionally, under specific coupling constants, the spin parameter may surpass the traditional Kerr bound. This suggests that black holes may possess higher spins than their classical counterparts [10].

From an astrophysical perspective, the rotating black hole with the type-A anomaly may have some observational features. With the Event Horizon Telescope collaboration already capturing images of

supermassive black holes at the centers of galaxies [11–13], studying black hole images, particularly the shadow of this black hole, becomes essential [14, 15]. The size and shape of a shadow can reflect the geometric structure and physical properties of the central black hole, thus having the potential to test the coupling parameter of the quantum-corrected black hole.

In this study, we investigate the observable features of the recently discovered black hole [1]. Specifically, our focus lies on the analysis of light rings (LRs) [16–19], shadows [20–24], and images when illuminated by an external light source [25–31]. Initially, we examine the effective potential of particles in the equatorial plane and derive the equation governing the positions of the LR. Due to the absence of an analytical solution, we numerically calculate the LR as a function of the coupling constant for various spin values. The existence of LR implies the presence of a critical curve and a shadow on the observer’s screen when illuminated by celestial light. To explore the shadow images, we employ the backward ray-tracing method. Furthermore, we utilize a simplified thin disk model to compare the intensity images with those of the Kerr black hole, aiming for a more realistic scenario.

The paper is organized as follows. In Sec. 2, we provide a review of the quantum-corrected Kerr black hole, examining particle trajectories and the existence of light rings within this spacetime. In Sec. 3, we investigate the shadow images of the quantum-corrected Kerr black hole when illuminated by a celestial source. Then, in Sec. 4, we introduce a thin disk model that serves as a more realistic light source, presenting the obtained results of black hole images. Finally, we summarize our findings and conclude this study in Sec. 5. We work in the geometrized unit with  $8\pi G = c = 1$  in this paper.

## 2 The metric and the light rings

To begin, let us briefly examine the semiclassical Einstein gravity with type-A anomaly and quantum-corrected Kerr black holes as described in [1]. In this framework, the background geometry remains classical while the quantum fields influence the geometry through their expectation value of the renormalized stress tensor, denoted as  $\langle T_{\mu\nu} \rangle$ , in the Einstein equations. It is worth noting that the trace of  $\langle T_{\mu\nu} \rangle$  is non-zero and dependent only on local curvature. If we consider the type-A trace anomaly, we have

$$g^{\mu\nu} \langle T_{\mu\nu} \rangle = \frac{\alpha}{2} \mathcal{G}, \quad (2.1)$$

where  $\mathcal{G} = R^2 - 4R_{\mu\nu}R^{\mu\nu} + R_{\mu\nu\rho\sigma}R^{\mu\nu\rho\sigma}$  is the Gauss-Bonnet scalar, and  $\alpha$  represents the coupling constant. By combining Eq. (2.1) with the semiclassical Einstein equations,  $R_{\mu\nu} - \frac{1}{2}g_{\mu\nu}R = \langle T_{\mu\nu} \rangle$ , we arrive at the following result:

$$\mathcal{R} = \frac{\alpha}{2} \mathcal{G}. \quad (2.2)$$

In general, it is typically impossible to solve the semiclassical Einstein equations when the renormalized stress tensor remains undetermined. However, in a fascinating discovery, the author of [1] was able to find a stationary and axisymmetric solution by adopting a Kerr-Schild ansatz and directly solving Eq. (2.2). These solutions can be interpreted as quantum-corrected Kerr black holes. The initial line-element was originally written in the ingoing Kerr-like coordinate system  $(\nu, r, \theta, \varphi)$ . For the sake of simplicity in our study, we will transform this into the BL coordinates  $(t, r, \theta, \Phi)$ ,

$$d\nu = dt + \frac{r^2 - a^2}{\Delta} dr, \quad d\varphi = \phi + \frac{a}{\Delta} dr, \quad (2.3)$$

$$ds^2 = -\frac{\Delta}{\Sigma} (dt - a \sin^2 \theta d\phi)^2 + \Sigma \left( \frac{dr^2}{\Delta} + d\phi^2 \right) + \frac{\sin^2 \theta}{\Sigma} [adt - (r^2 + a^2)d\phi]^2, \quad (2.4)$$

where  $\Delta = r^2 - 2\mathcal{M}r + a^2$ . We see that  $\mathcal{M}$  is the mass function introduced in Eq. (1.1). Since  $\mathcal{M}$  is dependent on  $\theta$ , the resulting spacetime does not satisfy the circularity conditions [32]. Fig. 1 provides various examples of  $\mathcal{M}$  under typical coupling constants. It is worth noting that a significant difference exists between the cases with positive and negative coupling constants. Additionally, the radius of the event horizon is also a function of  $\theta$ , which renders it non-spherically symmetric and requires numerical solving. Moreover, it has been observed that another Killing horizon is present at  $\Delta = 0$ . This horizon does not coincide with the primary horizon but is located quite close to it.

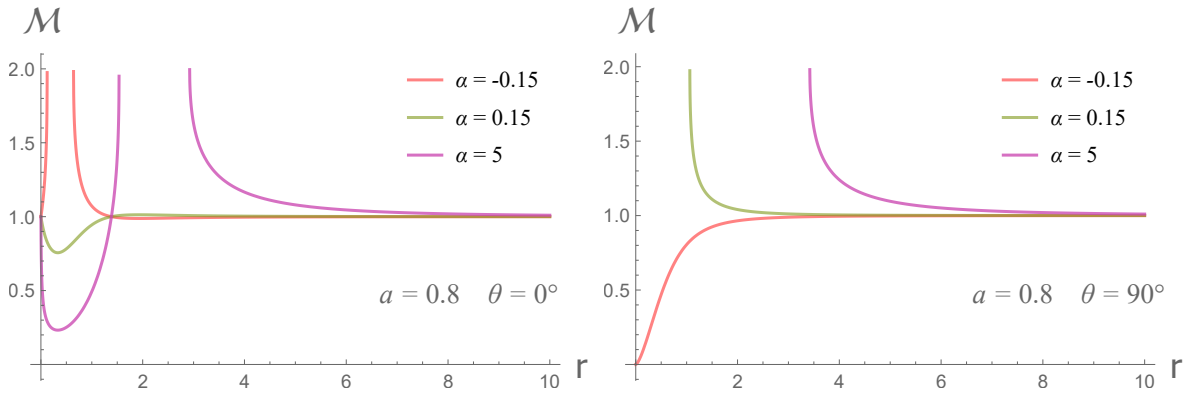


Figure 1:  $\mathcal{M}$  as function of  $r$  for different values of  $\alpha$ , evaluated at the pole (Left) and the equatorial plane (Right). The spin is fixed at  $a = 0.8$ .

The focus of our work is on particle motions around the quantum-corrected Kerr black hole. Specifically, we are interested in null geodesics since they are a crucial component of the observational properties associated with black holes. The constrained Hamiltonian for a point particle is given by

$$\mathcal{H} = \frac{1}{2} g_{\mu\nu} p^\mu p^\nu = -\frac{1}{2} m^2, \quad (2.5)$$

where  $p^\mu$  represents the momentum and  $m$  is the rest mass of the particle. As the spacetime we are dealing with is stationary and axisymmetric, the particle acquires a conserved energy  $E$  and angular

momentum  $L$  through the contraction of  $p_\mu$  with the Killing vectors  $\partial_t, \partial_\phi$ . However, due to the non-circular nature of the mass function in Eq. (1.1), it seems impossible to separate the equations of motion into first-order equations of  $r$  and  $\theta$  as can be done in Kerr spacetime. Nonetheless, we can still gain valuable physical insights by examining particle motions in the equatorial plane,  $\theta = \pi/2$ . In the case of equatorial motions, Eq. (2.5) reduces to

$$\left(\frac{dr}{d\lambda}\right)^2 = V_{eff}(r) = E^2 - m^2 + \frac{2\mathcal{M}m^2}{r} + \frac{a^2(E^2 - m^2) - L^2}{r^2} + \frac{2\mathcal{M}(L - aE)^2}{r^3}, \quad (2.6)$$

where we have defined an effective potential  $V_{eff}$  for convenience. Let us now focus on the case of photons with  $m = 0$ . The key property of photons is that their conserved energy can be absorbed into the affine parameter by rescaling  $\lambda \rightarrow \lambda E$ . Then, by defining  $l \equiv L/E$ , the effective potential becomes

$$V_{eff}(r) = 1 + \frac{a^2 - l^2}{r^2} + \frac{2\mathcal{M}(l - a)^2}{r^3}. \quad (2.7)$$

For photons, the unstable photon orbits, also known as light rings (LRs), are circular orbits of photons that play a crucial role in the observational properties of black holes. LRs can be obtained by setting

$$V_{eff} = 0, \quad \partial_r V_{eff} = 0. \quad (2.8)$$

From these equations, we obtain

$$l = -\frac{a\left(r^3 + 9r - 8\alpha + 6r^2\sqrt{1 - \frac{8\alpha}{r^3}}\right)}{r^3 - 9r + 8\alpha},$$

$$1 + \frac{a^2 - l^2}{r^2} + \frac{4(l - a)^2}{r^3\sqrt{1 - \frac{8\alpha}{r^3}}} = 0, \quad (2.9)$$

where and thereafter, for simplicity and without loss of generality, we set  $M = 1$ . Eq. (2.9) provides the equation for the LRs

$$1 + \frac{16a^2\left(r^3 - 8\alpha + 3r^2\sqrt{1 - \frac{8\alpha}{r^3}}\right)^2}{r^3(r^3 - 9r - 8\alpha)^2\left(1 + \sqrt{1 - \frac{8\alpha}{r^3}}\right)} + \frac{a^2}{r^2} - \frac{a^2\left(r^3 + 9r - 8\alpha + 6r^2\sqrt{1 - \frac{8\alpha}{r^3}}\right)^2}{r^2(r^3 - 9r - 8\alpha)^2} = 0. \quad (2.10)$$

As Eq. (2.10) is somewhat complicated, performing analytical calculations can be difficult; therefore, we solve the LRs numerically. There are two real roots,  $r_p, r_m$ , which correspond to prograde and retrograde photon orbits, respectively. It has been confirmed that these LRs are unstable under radial perturbations, that is,  $\partial_r^2 V_{eff} > 0$ . Consequently, similar to the Kerr spacetime, the LRs in the quantum-corrected Kerr solution imply a *shadow* region in the image of such black hole, which is studied and discussed in the next section.

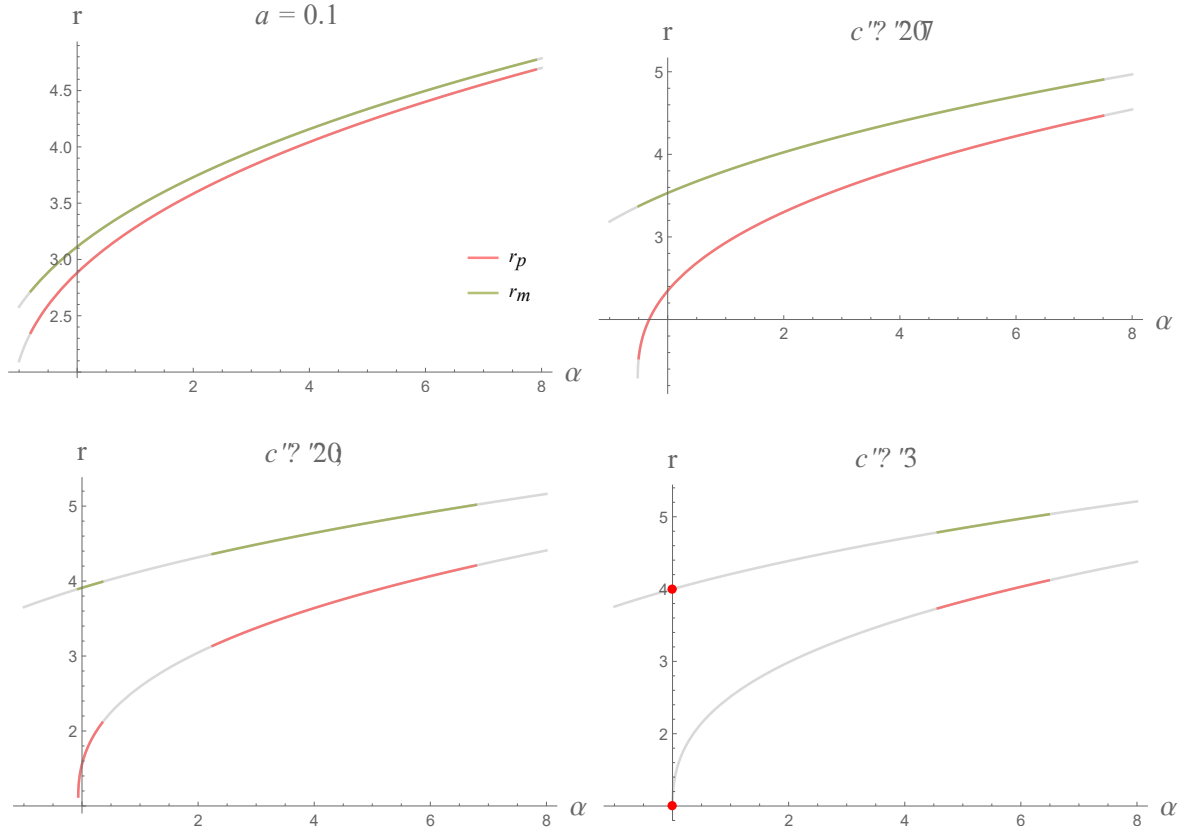


Figure 2: LR radii as functions of  $\alpha$ , under different spin parameters. The red and orange colors denote the prograde orbit and retrograde orbit, respectively.

Fig. 2 illustrates how the radii of LR radii change as the coupling constant  $\alpha$  increases, while the spin parameter remains fixed at different values. It's worth noting that although Eq. (2.10) has solutions throughout the range of  $-1 \leq \alpha \leq 8$ , only the colored parts of the curves correspond to the actual black hole solution, i.e., where the event horizon encloses the curvature singularities. The gray portions of the curves correspond either to cases where the event horizon is complex or where the singularity crosses the event horizon. For the case of  $a = 0.9$  (bottom right), there are two distinct intervals for black hole solutions:  $-0.0649 \leq \alpha \leq 0.3487$  and  $2.25 \leq \alpha \leq 6.784$ , consistent with the domain of black hole solutions found in [1]. In the case of  $a = 1$  (bottom left), the black hole touches the Kerr bound, and a black hole still exists for  $\alpha = 0$  (red dots) and  $4.5698 \leq \alpha \leq 6.47976$ . Anyway, it is apparent that both  $r_p$  and  $r_m$  increase with  $\alpha$ . This implies that a larger value of  $\alpha$  could potentially result in a larger shadow in the black hole image. This finding aligns with previous research studies [5, 6, 33].

### 3 Shadows cast by a celestial light source

It is known that the LRs affect the observational signature of a black hole significantly. Photons launched near these unstable orbits complete multiple loops around the black hole before reaching the observer, which leads to the formation of a critical curve in the observer's screen [34]. To investigate this characteristic of the quantum-corrected Kerr black hole, we utilize a celestial light source to illuminate the black hole. The center of the black hole is located at the origin, and its radius is much smaller than that of the event horizon or the distance between the observer and the black hole [35]. This setup allows the celestial source to outline the critical curve accurately and reveal the unstable photon orbits. When illuminated by the celestial source, any spacetime information that lies behind the LRs remains invisible on the screen. Light rays that penetrate the interior of the prograde LR  $r_p$  are inevitably captured by the black hole, creating a shadow region on the screen.

Once the celestial model is established, we utilize our backward ray-tracing method, developed in [35], to generate images of the black hole. The numerical strategy involves setting up a camera model at the observer and integrating the equations of motion along the null geodesics moving backward from the observer. To achieve this, we employ a fisheye camera model that incorporates the stereographic projection of the momentum  $p_\mu$  of photons onto the screen. For additional details, refer to [35]. With the values of  $p_\mu$  on the screen already determined, we may now proceed with determining the trajectories of the photons by performing backward integration of the Hamiltonian equations,

$$\frac{\partial \mathcal{H}}{\partial p_\mu} = \dot{x}^\mu, \quad \frac{\partial \mathcal{H}}{\partial x^\mu} = -\dot{p}_\mu, \quad (3.1)$$

where the dot denotes the derivative concerning the affine parameter for null geodesics. During the ray-tracing process, light rays that reach the celestial sphere are colored based on their positions. Rays that reach the horizon are colored black, creating a shadow region on the screen.

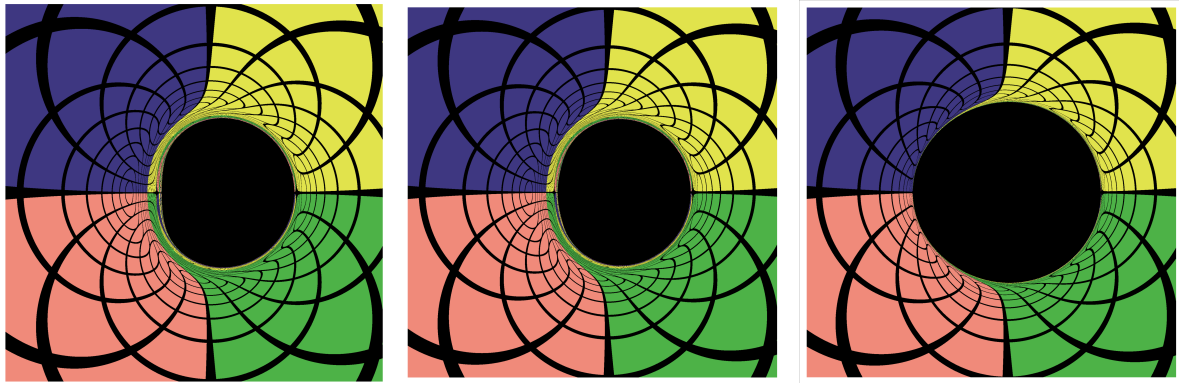


Figure 3: Black hole images of  $a = 0.99$  with  $\alpha \geq 0$ . Left:  $\alpha = 0$ , which corresponds to a near extreme Kerr black hole. Middle:  $\alpha = 0.02$ . Right:  $\alpha = 6.2$ . The observer is placed at  $r_o = 300$ ,  $\theta_o = \pi/2$ .

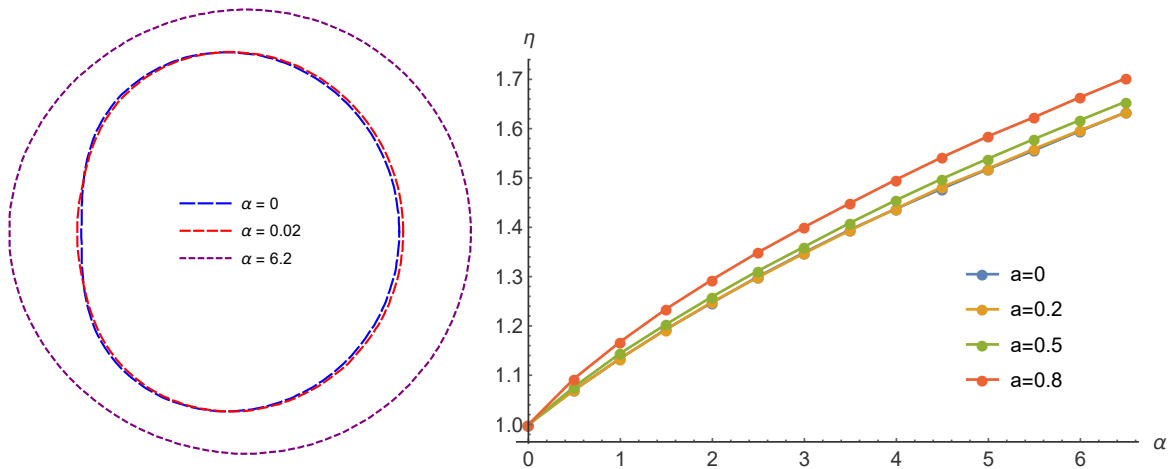


Figure 4: Left: shadow curves of black holes with  $a = 0.99$  and  $\alpha \geq 0$ . Right: the variation of the area ratio  $\eta$  with respect to positive  $\alpha$  for different black hole spin  $a$ . The incline angle of the observer is fixed at  $\theta_o = \pi/2$ .

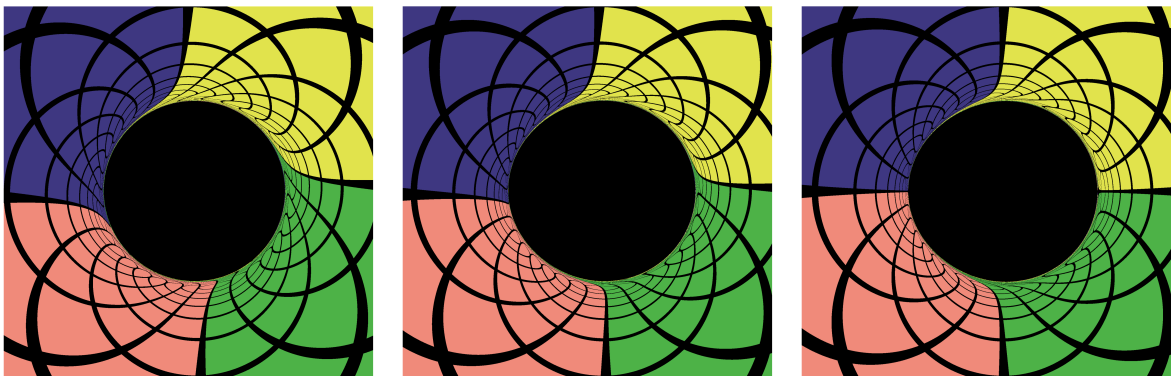


Figure 5: Black hole images of  $a = 1.06$  and  $\alpha = 6.275$ , which violates the Kerr bound  $a \leq 1$ . The observer is placed at  $r_o = 300$ . And the incline angles of the observer are  $\theta_o = \pi/9, \pi/3, \pi/2$ , respectively.

Let us first consider the case of  $\alpha \geq 0$ . Fig. 3 displays black hole images for three different positive values of  $\alpha$ , with an identical black hole spin  $a = 0.99$  for an edge-on observer ( $\theta_o = \pi/2$ ). It is evident that the black hole shadow increases in size due to the impact of a positive  $\alpha$ . As  $\alpha$  becomes sufficiently large, the shadow shape transforms into an ellipse as demonstrated in the right panel of Fig. 3. Moreover, regarding the case of large  $\alpha$ , the lensed images surrounding the shadow become narrower, which may indicate a different gravitational lensing process compared to that in typical Kerr spacetime. To quantify the impact of quantum corrections on the shadow, we introduce a parameter  $\eta \equiv S_{\text{BH}}/S_{\text{Kerr}}$ , representing the area ratio between the shadow of a quantum-corrected black hole and that of a Kerr black hole with identical spin. The right panel of Fig. 4 shows the variation of  $\eta$  concerning  $\alpha$  under different black hole spins. The area ratio  $\eta$  progressively increases as the



quantum-corrected parameter grows, with a more substantial impact on higher-spin black holes. This finding aligns with the behavior of the LRs, whose radii are monotonically increasing functions of  $\alpha$ . Furthermore, as illustrated in Fig. 5, we present an example of a violation of the Kerr bound, where  $a = 1.06$  and  $\alpha = 6.275$ , which is close to the maximum value found in [1]. However, we do not observe a remarkable feature compared to the right panel of Fig. 3, where  $a = 0.99$  and  $\alpha = 6.2$ . It is possible that the quantum corrections suppress the high-spin effect, even when it surpasses the Kerr bound.

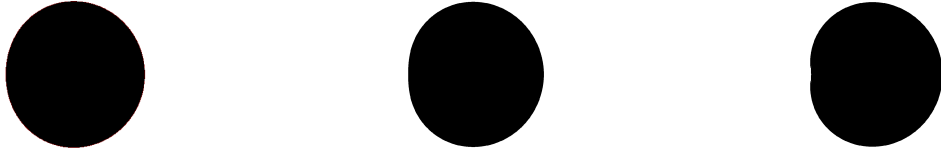


Figure 6: Black hole shadows of  $a = 0.8$  with  $\alpha \leq 0$ . Left:  $\alpha = 0$ , which corresponds to a Kerr black hole. Middle:  $\alpha = -0.09$ . Right:  $\alpha = -0.15$ . The observer is placed at  $r_o = 300$ ,  $\theta_o = \pi/2$ .

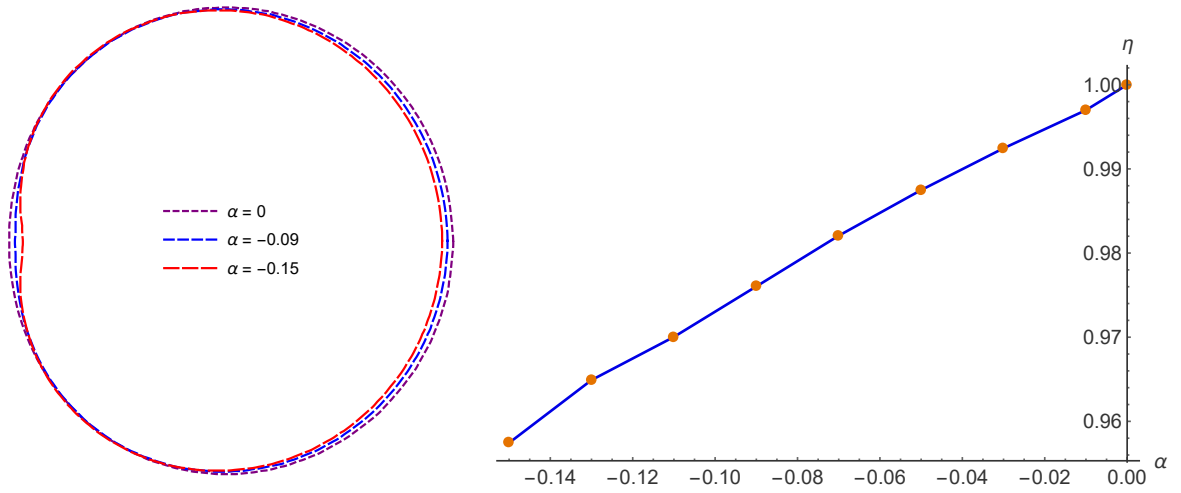


Figure 7: Left: shadow curves of black holes with  $a = 0.8$  and  $\alpha \leq 0$ . Right: the variation of the area ratio  $\eta$  with respect to negative  $\alpha$ . The black hole spin is fixed at  $a = 0.8$  and the incline angle of the observer is fixed at  $\theta_o = \pi/2$ .

Next, we proceed to the case of  $\alpha \leq 0$ . For clarity, we present the black hole shadows for three different values of  $\alpha$ , but with the same spin  $a = 0.8$  for an edge-on observer. The results are shown in Fig. 6. Here, we choose a smaller spin than that of the case with  $\alpha \geq 0$ , since the high spin limits the range of values for  $\alpha$ , as shown in Fig. 2 of [1]. As  $\alpha$  decreases, the left-hand side of the shadow

curve exhibits a concave shape, as seen in the right panel of Fig. 6 and the left panel of Fig. 7. Due to such effect, the shadow area may decrease as  $\alpha$  decreases. To verify this, we plot the variation of the area ratio  $\eta$  concerning  $\alpha$  in this case in Fig. 7. The range of  $\alpha$  follows the domain of existence for a black hole. By combining Fig. 7 with Fig. 4, we conclude that the area ratio  $\eta$  is a monotonically increasing function concerning the quantum-corrected parameter  $\alpha$ , similar to the radii of LRs.

Moreover, in the case of a nearly extreme Kerr black hole, an edge-on observer can observe a vertical line segment within the left contour of the shadow, as depicted in the left panel of Fig. 3. This vertical line, known as the NHEKline [36], originates from photons emitted in the near-horizon-extreme-Kerr (NHEK) geometry of the Kerr spacetime [36–38]. The existence of the NHEK geometry is attributed to the degeneracy of the inner and outer horizons [37]. However, the presence of the quantum-corrected parameter  $\alpha$  breaks the global degeneracy of the horizons, thereby destroying the NHEK geometry. As demonstrated in the left panel of Fig. 4, NHEKlines can be blurred by even a small value of  $\alpha$ .

## 4 Black hole images with a thin accretion disk

An astrophysical black hole is usually surrounded by an accretion disk. In this section, we utilize a simple disk model, similar to the one employed in [28], to generate images of the black hole-disk system. The disk is geometrically and optically thin, placed on the equatorial plane. The accretion flows are divided into two parts by the innermost stable circular orbit (ISCO), whose radius is determined by solving the following equations:

$$V_{eff}|_{r=r_{\text{ISCO}}} = 0, \quad \partial_r V_{eff}|_{r=r_{\text{ISCO}}} = 0, \quad \partial_r^2 V_{eff}|_{r=r_{\text{ISCO}}} = 0, \quad (4.1)$$

where  $V_{eff}$  is given by Eq. (2.6) with  $m = 1$ . The above equations are quite complicated, and the radius of the ISCO can only be solved numerically. Outside the ISCO, the accretion flows move along timelike circular orbits, whose four-velocities can be written as:

$$u^\mu = u_{\text{out}}^t(1, 0, 0, \Omega_s), \quad (4.2)$$

where

$$u_{\text{out}}^t = \sqrt{-\frac{1}{g_{\phi\phi}\Omega_s^2 + 2g_{t\phi}\Omega_s + g_{tt}}} \Big|_{\theta=\pi/2}, \quad \Omega_s = \frac{-\partial_r g_{t\phi} + \sqrt{(\partial_r g_{t\phi})^2 - \partial_r g_{\phi\phi} \partial_r g_{tt}}}{\partial_r g_{\phi\phi}} \Big|_{\theta=\pi/2}. \quad (4.3)$$

Inside the ISCO, the fluid falls from the ISCO to the event horizon, which means that the flows have the same conserved quantities as that for the ISCO. Hence, the components of the four-velocity take

the form:

$$\begin{aligned}
u_{\text{in}}^t &= (-g^{tt} E_{\text{ISCO}} + g^{t\phi} L_{\text{ISCO}}) \Big|_{\theta=\pi/2}, & u_{\text{in}}^\phi &= (-g^{t\phi} E_{\text{ISCO}} + g^{\phi\phi} L_{\text{ISCO}}) \Big|_{\theta=\pi/2}, \\
u_{\text{in}}^r &= -\sqrt{-\frac{g_{tt}u_{\text{in}}^t u_{\text{in}}^t + 2g_{t\phi}u_{\text{in}}^t u_{\text{in}}^\phi + g_{\phi\phi}u_{\text{in}}^\phi u_{\text{in}}^\phi + 1}{g_{rr}}} \Big|_{\theta=\pi/2}, & u_{\text{in}}^\theta &= 0,
\end{aligned} \tag{4.4}$$

where  $E_{\text{ISCO}}$  and  $L_{\text{ISCO}}$  is the conserved energy and angular momentum at the ISCO.

Light rays propagating around the black hole can undergo multiple crossings with the disk, leading to the accumulation of intensity. The expression for the observed intensity can be formulated as follows:

$$I_{\nu_o} = \sum_{n=1}^{N_{max}} g_n^3 J_n, \tag{4.5}$$

where  $\nu_o$  is the observed frequency on the screen,  $n = 1 \dots N_{max}$  is the number of times that the ray crosses the disk and  $N_{max}$  is the maximal crossing number,  $g_n$  is the corresponding redshift factor, and  $J_n$  denotes the emissivity at the  $n$ -th intersection point of the light ray with the disk. The emissivity is chosen as

$$J = \exp\left(-\frac{1}{2}z^2 - 2z\right), \quad z = \log\frac{r}{r_H}, \tag{4.6}$$

where  $r_H$  is the horizon radius on the equatorial plane.

The left column of Figure 8 illustrates the intensity maps obtained from thin disk imaging. In this case, the spin parameter is fixed at  $a = 0.99$ , and the observer is situated at  $r_o = 200$ ,  $\theta_o = 80^\circ$ . Within these intensity maps, the bright, narrow curves are referred to as ‘‘photon rings’’, which emerge due to the strong gravitational lensing effect. The shapes of these photon rings align with the shadows cast by the celestial light source mentioned earlier. Moreover, the completely dark regions central in the images result from the direct imaging of horizons, known as the ‘‘inner shadows’’ [39].

When comparing the two images in the left column of Figure 8, the most prominent distinction is that the quantum-corrected black hole exhibits a smaller inner shadow. To make a further investigation, we plot the maximal number of times light rays crossed the disk,  $N_{max}$ , as depicted in the middle column of Figure 8. Two notable differences are observed: First, the area occupied by light rays that do not intersect the disk is smaller in the image of a quantum-corrected black hole. As light rays accumulate intensity while passing through the disk, the inner shadow of a quantum-corrected black hole naturally appears diminished.

Second, for the quantum-corrected black hole, the regions corresponding to  $N_{max} = 2$  and  $N_{max} = 3$  have extended ‘‘tentacles’’ outward, which suggests that light rays are more likely to oscillate in their  $\theta$ -direction near the equatorial plane of the quantum-corrected black hole. We have analyzed the trajectories of light rays associated with the tentacles and observed that they predominantly

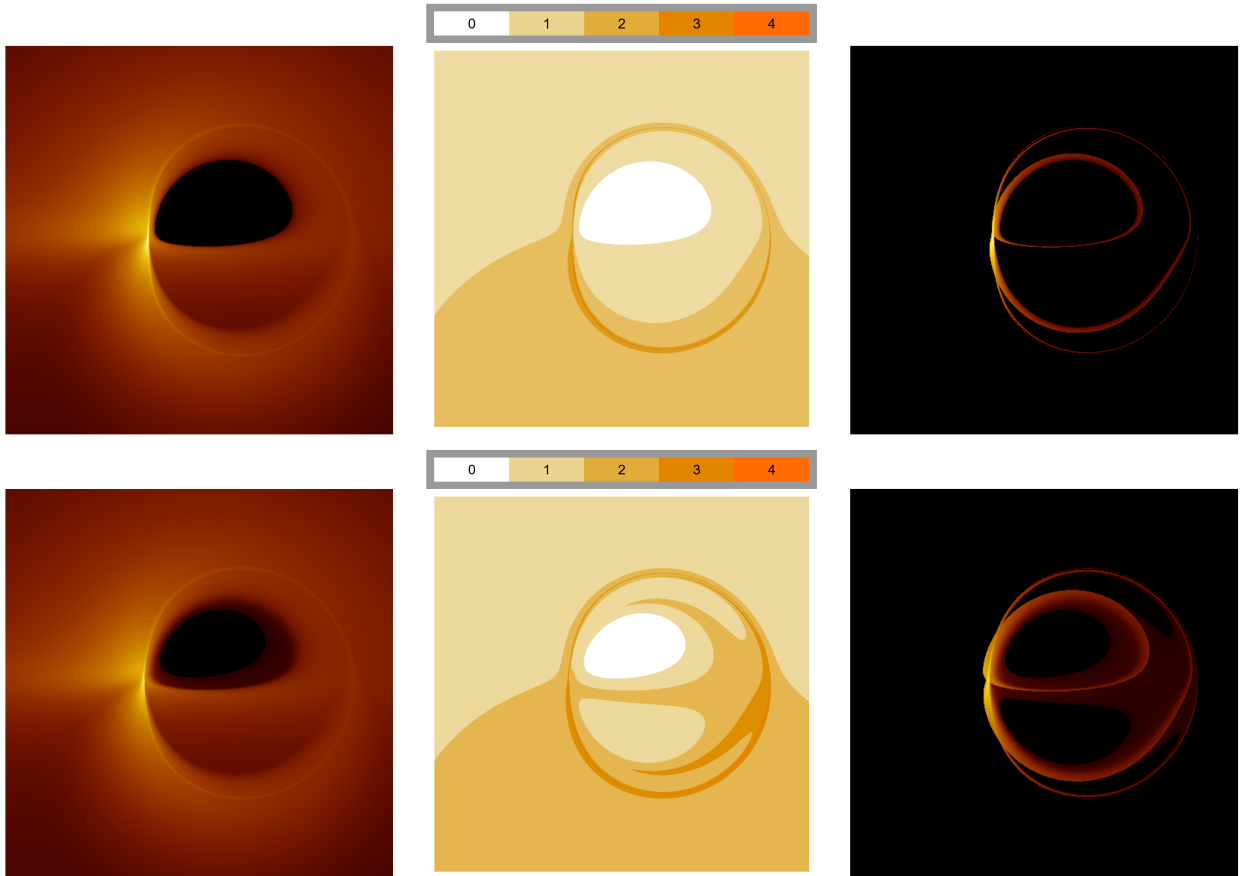


Figure 8: Black hole images illuminated by the thin disk model. The spin is set to be  $a = 0.99$ , and the observer is positioned at  $r_o = 200$ ,  $\theta_o = 80^\circ$ . The top row corresponds to a typical Kerr black hole with  $\alpha = 0$ , while the bottom row represents the quantum-corrected Kerr black hole with  $\alpha = 0.02$ . In the left column, we display the intensity maps generated by the thin disk. The middle column shows the number of times the light rays intersect the disk. Finally, the right column exhibits the intensity maps generated solely by the inner-ISCO region of the disk.

intersect the accretion disk between the ISCO and the horizon. This finding suggests that the non-circular spacetime effects resulting from quantum corrections are more pronounced in the vicinity of the horizon. In other words, the contribution of a near-horizon source plays a crucial role in the observable effects of a quantum-corrected black hole. To verify this, we present the imaging results in the right column of Fig. 8, where only the light source inside the ISCO is present. It is evident that the image of the quantum-corrected black hole differs significantly from that of a typical Kerr black hole.

It is worth noting that we have employed a phenomenological formula (4.6) for the emissivity when generating the images. Realistic millimeter-wave emissions are dominated by thermal synchrotron radiations, which are determined by the thermodynamics of the accretion flow. Although the con-

ventional disk model considers the ISCO as its inner boundary, there are also studies indicating that the accretion flow within the ISCO exhibits nontrivial dynamics and significant radiative capabilities [40]. Therefore, we may expect the presence of observable effects of quantum corrections in realistic accretion systems of black holes.

## 5 Summary and discussion

In this work, we focused on the observational signatures of the Kerr black hole solution in the semiclassical gravity with type-A trace anomaly [1]. Considering that the mass function  $\mathcal{M}$  depends both on  $r$  and  $\theta$ , the spacetime should be non-circular. Consequently, the Hamiltonian for a test particle does not allow for the separation of variables. To determine the radii of light rings, we performed numerical calculations based on the effective potential of photons. Our results consistently demonstrated that, for fixed values of  $a$  and  $\alpha$ , the radii of retrograde LRs are larger than those of prograde LRs, regardless of the sign of  $\alpha$ .

Furthermore, we confirmed that the light rings exhibit inherent instability in the radial direction, indicating the formation of a black hole shadow in the presence of a light source. We therefore assumed a celestial light source illuminating the black hole and utilized the backward ray-tracing technique to determine the shape and area of the shadow on the observer's screen. To characterize the variations in the shadow's area, we introduced the parameter  $\eta = S_{\text{BH}}/S_{\text{Kerr}}$ , representing the ratio of the shadow's area for a quantum-corrected black hole to that of a Kerr black hole with the same spin. Our findings revealed that as the parameter  $\alpha$  gradually increased within its range of values,  $\eta$  also increased. Moreover, an intriguing discovery was that the NHEKline was highly susceptible to disruption by  $\alpha$ . This phenomenon may arise from the fact that the presence of  $\alpha$  breaks the degeneracy between the inner and outer horizons, resulting in the absence of the NHEK geometry.

After that, we employed a simple disk model to study the black hole images in a more realistic manner. Our findings revealed that the images of the quantum-corrected black hole could deviate from those of the typical Kerr black hole. The primary factor causing this distinction is the quantum correction, which leads to a higher frequency of light ray oscillations around the equatorial plane, specifically between the ISCO and the horizon. As a result, the influence of a source near the horizon becomes crucial in determining the observable effects of a quantum-corrected black hole.

## Acknowledgments

We thank Prof. Bin Chen for the valuable discussions. The work is partly supported by NSFC Grant No. 12275004, 12205013 and 11873044. MG is also endorsed by "the Fundamental Research

Funds for the Central Universities” with Grant No. 2021NTST13.

## References

- [1] P. G. S. Fernandes, “Rotating black holes in semiclassical gravity,” [Phys. Rev. D](#) **108** no. 6, (2023) L061502, [arXiv:2305.10382 \[gr-qc\]](#).
- [2] D. M. Capper and M. J. Duff, “Trace anomalies in dimensional regularization,” [Nuovo Cim. A](#) **23** (1974) 173–183.
- [3] S. Deser and A. Schwimmer, “Geometric classification of conformal anomalies in arbitrary dimensions,” [Phys. Lett. B](#) **309** (1993) 279–284, [arXiv:hep-th/9302047](#).
- [4] R.-G. Cai, L.-M. Cao, and N. Ohta, “Black Holes in Gravity with Conformal Anomaly and Logarithmic Term in Black Hole Entropy,” [JHEP](#) **04** (2010) 082, [arXiv:0911.4379 \[hep-th\]](#).
- [5] M. Guo and P.-C. Li, “Innermost stable circular orbit and shadow of the 4D Einstein–Gauss–Bonnet black hole,” [Eur. Phys. J. C](#) **80** no. 6, (2020) 588, [arXiv:2003.02523 \[gr-qc\]](#).
- [6] X.-X. Zeng, H.-Q. Zhang, and H. Zhang, “Shadows and photon spheres with spherical accretions in the four-dimensional Gauss–Bonnet black hole,” [Eur. Phys. J. C](#) **80** no. 9, (2020) 872, [arXiv:2004.12074 \[gr-qc\]](#).
- [7] S. U. Islam, R. Kumar, and S. G. Ghosh, “Gravitational lensing by black holes in the 4D Einstein–Gauss–Bonnet gravity,” [JCAP](#) **09** (2020) 030, [arXiv:2004.01038 \[gr-qc\]](#).
- [8] R. A. Konoplya and A. F. Zinhailo, “Quasinormal modes, stability and shadows of a black hole in the 4D Einstein–Gauss–Bonnet gravity,” [Eur. Phys. J. C](#) **80** no. 11, (2020) 1049, [arXiv:2003.01188 \[gr-qc\]](#).
- [9] S. Tsujikawa, “Black holes in a new gravitational theory with trace anomalies,” [Phys. Lett. B](#) **843** (2023) 138054, [arXiv:2304.10019 \[gr-qc\]](#).
- [10] J. Jiang and M. Zhang, “Overspinning a rotating black hole in semiclassical gravity with type-A trace anomaly,” [arXiv:2305.12345 \[gr-qc\]](#).
- [11] **Event Horizon Telescope** Collaboration, K. Akiyama et al., “First M87 Event Horizon Telescope Results. I. The Shadow of the Supermassive Black Hole,” [Astrophys. J. Lett.](#) **875** (2019) L1, [arXiv:1906.11238 \[astro-ph.GA\]](#).

- [12] **Event Horizon Telescope** Collaboration, K. Akiyama *et al.*, “First Sagittarius A\* Event Horizon Telescope Results. I. The Shadow of the Supermassive Black Hole in the Center of the Milky Way,” [\*Astrophys. J. Lett.\* \*\*930\*\* no. 2, \(2022\) L12.](#)
- [13] R.-S. Lu *et al.*, “A ring-like accretion structure in M87 connecting its black hole and jet,” [\*Nature\* \*\*616\*\* no. 7958, \(2023\) 686–690, \[arXiv:2304.13252\]\(#\) \[\[astro-ph.HE\]\(#\)\].](#)
- [14] S. Vagnozzi *et al.*, “Horizon-scale tests of gravity theories and fundamental physics from the Event Horizon Telescope image of Sagittarius A,” [\*Class. Quant. Grav.\* \*\*40\*\* no. 16, \(2023\) 165007, \[arXiv:2205.07787\]\(#\) \[\[gr-qc\]\(#\)\].](#)
- [15] S. Chen, J. Jing, W.-L. Qian, and B. Wang, “Black hole images: A review,” [\*Sci. China Phys. Mech. Astron.\* \*\*66\*\* no. 6, \(2023\) 260401, \[arXiv:2301.00113\]\(#\) \[\[astro-ph.HE\]\(#\)\].](#)
- [16] P. V. P. Cunha, E. Berti, and C. A. R. Herdeiro, “Light-Ring Stability for Ultracompact Objects,” [\*Phys. Rev. Lett.\* \*\*119\*\* no. 25, \(2017\) 251102, \[arXiv:1708.04211\]\(#\) \[\[gr-qc\]\(#\)\].](#)
- [17] P. V. P. Cunha and C. A. R. Herdeiro, “Stationary black holes and light rings,” [\*Phys. Rev. Lett.\* \*\*124\*\* no. 18, \(2020\) 181101, \[arXiv:2003.06445\]\(#\) \[\[gr-qc\]\(#\)\].](#)
- [18] M. Guo and S. Gao, “Universal Properties of Light Rings for Stationary Axisymmetric Spacetimes,” [\*Phys. Rev. D\* \*\*103\*\* no. 10, \(2021\) 104031, \[arXiv:2011.02211\]\(#\) \[\[gr-qc\]\(#\)\].](#)
- [19] R. Ghosh and S. Sarkar, “Light rings of stationary spacetimes,” [\*Phys. Rev. D\* \*\*104\*\* no. 4, \(2021\) 044019, \[arXiv:2107.07370\]\(#\) \[\[gr-qc\]\(#\)\].](#)
- [20] M. Heydari-Fard, M. Heydari-Fard, and H. R. Sepangi, “Thin accretion disks around rotating black holes in 4D Einstein–Gauss–Bonnet gravity,” [\*Eur. Phys. J. C\* \*\*81\*\* no. 5, \(2021\) 473, \[arXiv:2105.09192\]\(#\) \[\[gr-qc\]\(#\)\].](#)
- [21] J. Peng, M. Guo, and X.-H. Feng, “Influence of quantum correction on black hole shadows, photon rings, and lensing rings,” [\*Chin. Phys. C\* \*\*45\*\* no. 8, \(2021\) 085103, \[arXiv:2008.00657\]\(#\) \[\[gr-qc\]\(#\)\].](#)
- [22] Z. Zhang, H. Yan, M. Guo, and B. Chen, “Shadows of Kerr black holes with a Gaussian-distributed plasma in the polar direction,” [\*Phys. Rev. D\* \*\*107\*\* no. 2, \(2023\) 024027, \[arXiv:2206.04430\]\(#\) \[\[gr-qc\]\(#\)\].](#)
- [23] Y. Meng, X.-M. Kuang, and Z.-Y. Tang, “Photon regions, shadow observables, and constraints from M87\* of a charged rotating black hole,” [\*Phys. Rev. D\* \*\*106\*\* no. 6, \(2022\) 064006, \[arXiv:2204.00897\]\(#\) \[\[gr-qc\]\(#\)\].](#)

- [24] A. He, J. Tao, P. Wang, Y. Xue, and L. Zhang, “Effects of Born–Infeld electrodynamics on black hole shadows,” [Eur. Phys. J. C](#) **82** no. 8, (2022) 683, [arXiv:2205.12779 \[gr-qc\]](#).
- [25] P. V. P. Cunha, N. A. Eiró, C. A. R. Herdeiro, and J. P. S. Lemos, “Lensing and shadow of a black hole surrounded by a heavy accretion disk,” [JCAP](#) **03** (2020) 035, [arXiv:1912.08833 \[gr-qc\]](#).
- [26] Z. Zhang, S. Chen, X. Qin, and J. Jing, “Polarized image of a Schwarzschild black hole with a thin accretion disk as photon couples to Weyl tensor,” [Eur. Phys. J. C](#) **81** no. 11, (2021) 991, [arXiv:2106.07981 \[gr-qc\]](#).
- [27] Y. Hou, P. Liu, M. Guo, H. Yan, and B. Chen, “Multi-level images around Kerr–Newman black holes,” [Class. Quant. Grav.](#) **39** no. 19, (2022) 194001, [arXiv:2203.02755 \[gr-qc\]](#).
- [28] Y. Hou, Z. Zhang, H. Yan, M. Guo, and B. Chen, “Image of a Kerr–Melvin black hole with a thin accretion disk,” [Phys. Rev. D](#) **106** no. 6, (2022) 064058, [arXiv:2206.13744 \[gr-qc\]](#).
- [29] X.-J. Wang, X.-M. Kuang, Y. Meng, B. Wang, and J.-P. Wu, “Rings and images of Horndeski hairy black hole illuminated by various thin accretions,” [Phys. Rev. D](#) **107** no. 12, (2023) 124052, [arXiv:2304.10015 \[gr-qc\]](#).
- [30] C. Zhang, Y. Ma, and J. Yang, “Black hole image encoding quantum gravity information,” [Phys. Rev. D](#) **108** no. 10, (2023) 104004, [arXiv:2302.02800 \[gr-qc\]](#).
- [31] S. Hu, C. Deng, S. Guo, X. Wu, and E. Liang, “Observational signatures of Schwarzschild-MOG black holes in scalar–tensor–vector gravity: images of the accretion disk,” [Eur. Phys. J. C](#) **83** no. 3, (2023) 264.
- [32] A. E. Héloïse Delaporte and A. Held, “Parameterizations of black-hole spacetimes beyond circularity,” [Classical and Quantum Gravity](#) **39** no. 13, (2022) 134002, [arXiv:2003.00105 \[gr-qc\]](#).
- [33] R. Kumar and S. G. Ghosh, “Rotating black holes in 4D Einstein–Gauss–Bonnet gravity and its shadow,” [JCAP](#) **07** (2020) 053, [arXiv:2003.08927 \[gr-qc\]](#).
- [34] S. E. Gralla, D. E. Holz, and R. M. Wald, “Black Hole Shadows, Photon Rings, and Lensing Rings,” [Phys. Rev. D](#) **100** no. 2, (2019) 024018, [arXiv:1906.00873 \[astro-ph.HE\]](#).
- [35] Z. Hu, Z. Zhong, P.-C. Li, M. Guo, and B. Chen, “QED effect on a black hole shadow,” [Phys. Rev. D](#) **103** no. 4, (2021) 044057, [arXiv:2012.07022 \[gr-qc\]](#).



- [36] S. E. Gralla, A. Lupsasca, and A. Strominger, “Observational Signature of High Spin at the Event Horizon Telescope,” [Mon. Not. Roy. Astron. Soc.](#) **475** no. 3, (2018) 3829–3853, [arXiv:1710.11112](#) [[astro-ph.HE](#)].
- [37] J. M. Bardeen and G. T. Horowitz, “The Extreme Kerr throat geometry: A Vacuum analog of  $AdS(2) \times S^2$ ,” [Phys. Rev. D](#) **60** (1999) 104030, [arXiv:hep-th/9905099](#).
- [38] Y. Hou, Z. Zhang, M. Guo, and B. Chen, “Electromagnetic effects on charged particles in a near-horizon-extreme-Kerr geometry,” [Phys. Rev. D](#) **107** no. 12, (2023) 124014, [arXiv:2301.08467](#) [[gr-qc](#)].
- [39] A. Chael, M. D. Johnson, and A. Lupsasca, “Observing the Inner Shadow of a Black Hole: A Direct View of the Event Horizon,” [Astrophys. J.](#) **918** no. 1, (2021) 6, [arXiv:2106.00683](#) [[astro-ph.HE](#)].
- [40] A. Mummery and S. Balbus, “Accretion within the innermost stable circular orbit: analytical thermodynamic solutions in the adiabatic limit,” [Mon. Not. Roy. Astron. Soc.](#) **521** no. 2, (2023) 2439–2463, [arXiv:2302.14437](#) [[astro-ph.HE](#)].